Nuclear Science and Techniques (2024) 35:201
https://doi.org/10.1007/s41365-024-01575-2

Performance of AC-LGAD strip sensors designed for the DarkSHINE experiment

Kang Liu[1,2] · Meng-Zhao Li[3,4,5] · Jun-Hua Zhang[1,2] · Wei-Yi Sun[3,5] · Yun-Yun Fan[3,4] · Zhi-Jun Liang[3,4] · Yu-Feng Wang[1,2] · Mei Zhao[3,4] · Kun Liu[1,2,6]

Received: 18 April 2024 / Revised: 18 July 2024 / Accepted: 28 July 2024 / Published online: 14 October 2024

Abstract
The DarkSHINE experiment proposes a novel approach to single-electron-on-fixed-target exploration that focuses on the search for dark photons through their invisible decay into dark matter particles. Central to this initiative is an advanced tracking detector designed to achieve exceptional sensitivity in the detection of light dark matter candidates. This study evaluates the performance of several prototype AC-coupled low-gain avalanche diode (AC-LGAD) strip sensors specifically developed for the DarkSHINE tracking detector. The electrical properties of the sensors from two batches of wafers with different n^+ doses are thoroughly evaluated. Spatial and temporal resolutions are measured using an infrared laser source. The spatial resolutions range from 6.5 to 8.2 μm and from 8.8 to 12.3 μm for the sensors from two distinct dose batches, each with a 100 μm pitch size. Furthermore, the sensors demonstrate time resolutions of 8.3 and 11.4 ps, underscoring the potential of AC-LGAD technology in enhancing the performance of the DarkSHINE tracking detector.

Keywords The DarkSHINE experiment · Silicon-strip detector · AC-LGAD sensor · Spatial resolution · Timing resolution

1 Introduction

Experimental observations and theoretical research in astrophysics and cosmology indicate that the Universe contains approximately 68% dark energy and 27% dark matter, whereas ordinary matter described by the particle-physics standard model (the so-called visible baryonic matter) constitutes only 5% of the total energy of the Universe. Despite the increasing astronomical evidence supporting the existence of dark matter, little is known about its nature. Dark matter does not participate in electromagnetic interactions; thus, detecting dark matter particles experimentally is challenging. Over the past few decades, dark matter detection experiments have been conducted worldwide, with the primary goal of searching for weakly interacting massive particles (WIMPs). These experiments include direct

Kang Liu and Meng Zhao Li have contributed equally to this work.

This work was supported by the National Natural Science Foundation of China (No. 12150006), Shanghai Pilot Program for Basic Research - Shanghai Jiao Tong University (No. 21TQ1400209), and the Young Talents of National Talent Support Programs (No. 24Z130300579).

✉ Yu-Feng Wang
yufeng.wang@sjtu.edu.cn

✉ Mei Zhao
zhaomei@ihep.ac.cn

✉ Kun Liu
kun.liu@sjtu.edu.cn

1 Tsung-Dao Lee Institute, Shanghai Jiao Tong University, Shanghai 201210, China

2 Key Laboratory for Particle Astrophysics and Cosmology (MOE), Shanghai Key Laboratory for Particle Physics and Cosmology (SKLPPC), Shanghai 200240, China

3 Institute of High Energy Physics, Chinese Academy of Sciences, Beijing 100049, China

4 State Key Laboratory of Particle Detection and Electronics, Institute of High Energy Physics, Chinese Academy of Sciences, Beijing 100049, China

5 University of Chinese Academy of Sciences, Beijing 100049, China

6 Institute of Nuclear and Particle Physics, School of Physics and Astronomy, Shanghai Jiao Tong University, Shanghai 200240, China

detection experiments such as the PandaX [1], CDEX [2], and XENONnT [3] experiments; dark matter production experiments such as the ATLAS [4] and CMS [5] experiments at the Large Hadron Collider; and space experiments such as the DAMPE [6] and AMS [7] experiments. These experiments are competitive, continuously pushing the upper limits of the interaction cross section of dark matter particles with ordinary matter in the mass range of GeV to tens of TeV. However, the detection of light dark matter candidates in the sub-GeV (from MeV to GeV) mass range, which is equally important, remains relatively weak. Therefore, the development of new detection methods for light dark matter particles in the sub-GeV mass range has been incorporated into the European Particle Physics Strategy 2020 [8] and U.S. Snowmass Strategy 2021 [9]. Dark photons, as mediator particles for interactions between dark matter particles, are also considered candidate particles for light dark matter [10–16]. They can dynamically mix and convert into photons, serving as a portal connecting the world of dark matter to that of ordinary matter. Therefore, the search for dark photons in the sub-GeV mass range is a promising breakthrough in identifying dark matter particles [17–21].

The DarkSHINE experiment is a newly proposed electron-on-fixed-target experiment that searches for dark photon particles produced via electron and nucleon interactions. The dark photons then decay into a pair of dark matter candidates, which is known as invisible decay [22]. Dark matter pairs escape detection with missing momentum and energy, resulting in a lower momentum and larger recoil angle of the recoil electron. The missing momentum signature is used to identify signals from various Standard Model background processes. The under-construction LCLS-II facility [23–25] based at the US SLAC National Accelerator Laboratory and the Shanghai High Repetition-Rate XFEL and Extreme Light Facility (SHINE) [26–29] based in Shanghai were designed to conduct high-repetition-rate electron beams, enabling precise detection of the dark photon invisible decay process. The DarkSHINE experiment plans to use the single electron beam provided by the SHINE facility. Compared to typical beam-dump experiments, the DarkSHINE experiment is highly sensitive to dark photons and sub-GeV dark matter candidates [30]. To detect the missing momentum, the reconstruction of the position and momentum of the incident and recoil electrons is crucial for this experiment.

To achieve such high sensitivity, the detector of the DarkSHINE experiment was designed as shown on the left of Fig. 1. By design, a single electron bunch is provided every 60 ns through the DarkSHINE kicker system in the SHINE linac. The tracking system is placed in a downward magnetic field of approximately 1.5 T, which is provided by a superconducting magnet system. As shown in the plots on the right of Fig. 1, the DarkSHINE tracking system consists of seven layers of tagging modules and six layers of recoil modules, and a tungsten target with a $0.1X_0$ decay length is placed between them. The magnetic-field direction is defined as the *y*-direction and the electron-beam direction as the *z*-direction; hence, the electron is deflected in the *x*-direction perpendicular to the magnetic field. Each layer of the tracking module consists of two silicon sensors with lengths of at least 20 mm placed at a small angle (100 mrad) along the y-direction. The sensors are expected to be as thin as possible to avoid multitrack events caused by the interaction between the charged particles and the nucleus of the detector material. The designed position (angle) resolution of the

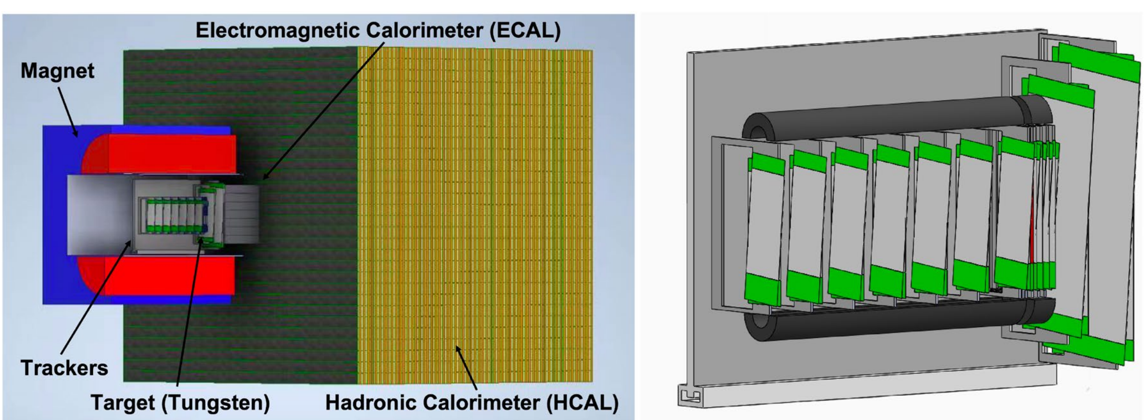

Fig. 1 (Color online) Left: Schematic of the detector used in the DarkSHINE experiment [30]. Along the incident direction of the electron, from left to right in the picture, the red material with a blue brace is the dipole magnet. The tagging tracker is placed at the center of the magnet. The recoil tracker is located at the edge of the magnet, and the target is caught in the middle. ECAL is placed after the recoil tracker, followed by HCAL. Right: Schematic of the DarkSHINE tracking system. From left to right: tagging tracker (with seven layers of tracking modules), tungsten target, and recoil tracker (with six layers of tracking modules). For each layer, two strip sensors are shown in the diagram, placed at a small angle (100 mrad)

tracking system is better than 10 μm in the direction of electron deflection. To achieve this, several small prototype sensors have been designed using AC-coupled low-gain avalanche diodes (AC-LGADs, also called resistive silicon detectors).

The LGAD [31, 33–37] was developed in recent years as a novel precise detector technology, initially proposed and designed for precise timing measurements. It has been used for the high-granularity timing detector of ATLAS [38] and endcap timing layer of CMS [39] for the High-Luminosity Large Hadron Collider. The left plot of Fig. 2 shows a schematic of an LGAD sensor. The LGAD sensors are fabricated on high-resistivity p-type substrates with thicknesses of approximately 50 μm. Based on traditional n-in-p silicon sensors, the LGAD sensor has an additional highly doped p^+ region (namely, the "gain layer") under the parallel n-p junction. When a bias voltage is applied across the sensor, the p^+ layer is depleted and creates a strong local electric field, thereby introducing internal gain. To achieve better spatial resolution while maintaining a similar gain and fast timing performance, AC-LGAD technology has been used where the signal is capacitively induced and shared among metal AC pads. The right plot of Fig. 2 shows a sketch of an AC-LGAD sensor. The AC pads of the sensor used for the signal readout are placed on a thin dielectric layer grown over the n^+ layer of the sensor. The n^{++} layer in the standard LGADs is replaced by a much less doped n^+ layer in the AC-LGADs. This results in increased inter-pad resistance [40]. A highly doped n^{++} implant is preserved at the edge of the active area of the sensor to provide a DC connection for electron-current draining. The AC-LGAD design can be easily adapted to any detector geometry because segmentation can be achieved using AC pads of any shape.

To meet the spatial-resolution requirement and study the performance of the detector, three types of strip sensors with pitch (strip) sizes of 100 (50) μm, 60 (40) μm, and 45 (30) μm were designed for the DarkSHINE experiment, where the strip size refers to the width of the metal strips and electrodes. Two batches of wafers of AC-LGAD strip-sensor prototypes were produced by the Institute of Microelectronics of the Chinese Academy of Sciences, based on the AC-LGAD technology designed by the Institute of High Energy Physics of the Chinese Academy of Sciences (IHEP). They are referred to as the wafer-11 and wafer-12 sensors hereafter. The n^+ doses of these two wafers are 0.01 P and 10 P, respectively, where P is the unit of phosphorus dose defined for the AC-LGADs. Further details are available in [31]. Figure 3 shows a design drawing and photograph of the fabricated AC-LGAD strip-sensor prototype. The sensor size is 3638 μm × 3638 μm and each metal strip has a length of 2000 μm. The sensors have three rings (from the outside to the inside): the outer ring, guard ring, and DC ring. The sensors have a 50 μm epitaxial layer and 725 μm substrate.

This study presents the performance tests of the AC-LGAD prototype strip sensors with pitch (strip) sizes of 100 (50) μm. Their electrical characteristics are studied using a probe station, and the measurements are presented in Sect. 2. The sensors were tested using a laser source to measure their position-reconstruction and spatial-resolution performances. Further details are presented in Sect. 3. The timing performance is also tested, and the results are presented in Sect. 4.

2 *I–V* and *C–V* performance test

Performance tests for both the *I–V* and *C–V* characteristics are conducted within the probe station in a clean-room infrastructure at Shanghai Jiao Tong University. The sensor is placed on the surface of the chunk in the probe station, and a significant bias voltage is applied to the chunk. The guard ring of the sensor is continuously grounded during the test to guarantee the integrity of the test conditions. For the *C–V* curve measurement, a dedicated four-channel (low current (LC), low potential (LP), high current (HC), and high potential (HP)) high-voltage adapter is connected in parallel between the sensor and LCR meter [41]. This setup effectively regulates the voltage to maintain it within a safe operating range, thereby safeguarding the equipment and ensuring accurate measurements. Following the recommendations of RD50 [42], the LCR meter is operated at a frequency of 10 kHz to enhance the reliability and consistency of the

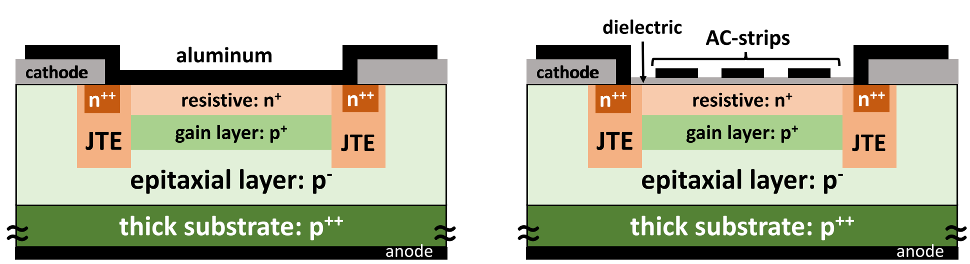

Fig. 2 (Color online) Left: Schematic of a section of a single-pad standard LGAD. Right: Schematic of a section of a segmented AC-LGAD sensor [40]. The schematics are not to actual scale

results. The sensor must be kept in a dark-room environment without interference from any external light source during the entire measurement period to reduce the light-induced leakage current.

2.1 Current–voltage measurement

The measured *I*–*V* performance of wafer-11 and wafer-12 is shown in Fig. 4. A plateau current for wafer-11 is observed below 1 nA, whereas for wafer-12, the current reaches 100 nA. Additionally, the breakdown voltage (V_{BD}), defined as the reverse bias voltage applied when the leakage current reaches 500 nA, is approximately 380 V (185 V) for the wafer-11 (wafer-12) sensors under room-temperature conditions (25°C). This discrepancy in performance is attributed to the small variance in the gain-layer dose between the two wafers. In addition, wafer-12 is carbon doped for radiation resistance, which leads to a larger leakage current under the same bias voltage compared to wafer-11.

The investigation is further extended to the temperature dependence of the *I*–*V* performance, as shown in the left plot of Fig. 5. The *I*–*V* curves are recorded at different temperatures: (5°C), (15°C), (25°C), and (30°C). A discernible trend emerges wherein both the current and V_{BD} increase with increasing temperature, which is attributed to the augmented thermal motion of the electron-hole pairs. Consequently, this observation necessitates prudent consideration when setting the working voltage of the wafer-11 (wafer-12) sensors below 350 V (150 V), ensuring optimal operational parameters. Finally, the consistency of the n$^+$-doping distribution within the active region of the AC-LGAD sensors is checked. As shown in the right plot of Fig. 5, small variations in the leakage current are observed, minutely shifting according to the specific position of the sensor on the wafer owing to the inherent nonuniformity in doping.

2.2 Capacitance–voltage measurement

The capacitance–voltage (*C*–*V*) curves provided valuable insights into the operational characteristics of the multiplication layer embedded within the AC-LGAD sensors. These sensors are tested under standard room-temperature conditions, with the applied bias voltage scanned in precise 1 V increments. The graphical representation shown in the left plot of Fig. 6 presents a comprehensive display of the measured *C*–*V* curves for one wafer-11 sensor and three distinct wafer-12 sensors, offering a detailed examination of their performance. Similarly, the right plot of

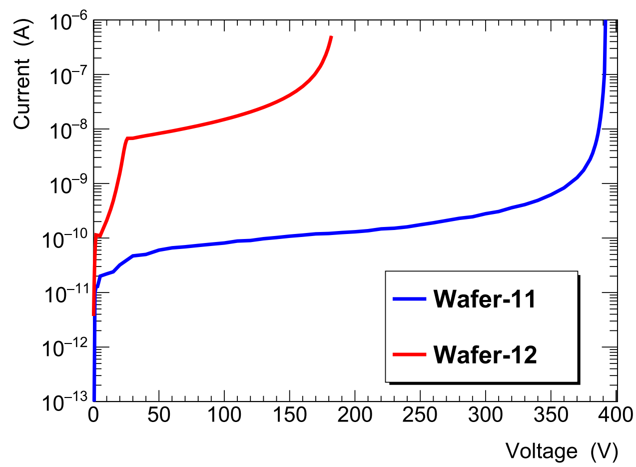

Fig. 4 (Color online) Current–voltage performance of two AC-LGAD sensors from wafer-11 (blue) and wafer-12 (red)

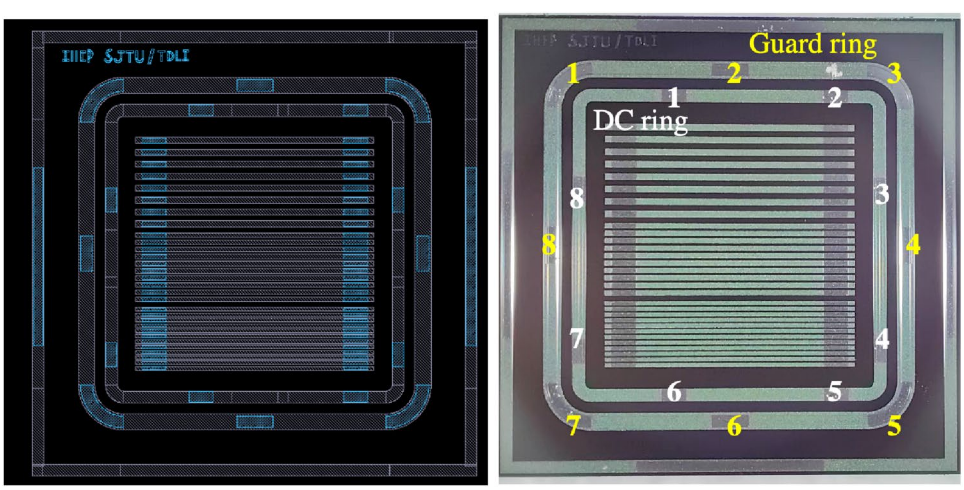

Fig. 3 (Color online) Left: Design of the AC-LGAD strip sensor for the DarkSHINE experiment. Right: Image of the silicon strip sensor under a microscope (size of 3638 × 3638 μm)

Fig. 6 shows the corresponding $1/C^2$ curves, offering a deeper understanding of the underlying dynamics.

No discernible deviations are observed in the C–V curves, which implies that the small nonuniformity in doping across the wafers has a negligible impact on the overall junction capacitance. The distinctive features exhibited by the $1/C^2 - V$ curves, which show two plateaus, are notable. These plateaus serve as key indicators for identifying parameters such as the gain-layer depletion voltage (V_{GL}) and full-depletion voltage (V_{FD}) through analysis of the $1/C^2$–V curves. V_{GL}, the turning point where the $1/C^2 - V$ curves commence their ascent after the initial plateau, is intricately linked to the peak of the n$^+$-doping density. For the wafer-11 and wafer-12 sensors, V_{GL} is estimated to be approximately 20 V and 24 V, respectively, signaling the complete depletion of their gain layers. However, V_{FD}, which marks the voltage at which the curves plateau after reaching full depletion, provides insights into the sensor behavior. Following the depletion of the gain layer, the slopes of the curves for both the wafer-11 and wafer-12 sensors exhibit great similarity owing to their identical bulk resistivity.

The observed stabilization of V_{FD} at approximately 40 V for both the wafer-11 and wafer-12 sensors demonstrates their consistent behavior despite potential manufacturing variations. This result not only improves our understanding of the complex dynamics governing sensor behavior, but also provides a basis for optimizing fabrication processes across different operational conditions and applications.

3 Position-reconstruction and spatial-resolution test

The position reconstruction performance of the silicon-strip detector is key to the DarkSHINE experiment. These aspects are investigated using a laser system with precisely defined positions. This section provides detailed documentation of the experimental setup, methods employed for position-reconstruction and spatial-resolution determination, and the evaluation techniques utilized.

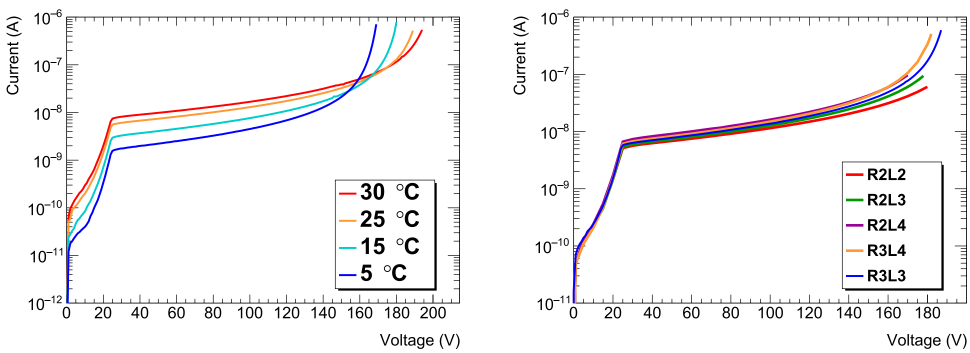

Fig. 5 (Color online) Left: Current–voltage temperature dependency of wafer-12 sensors. Right: Curves with different colors represent sensors from different positions on the wafer; R indicates the row and L indicates the column of the sensor

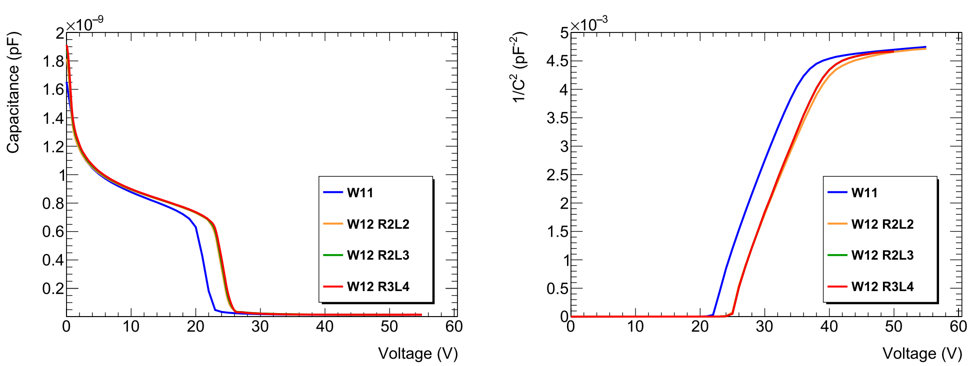

Fig. 6 (Color online) Capacitance–voltage and $1/C^2 - V$ curves of the prototype strip sensors measured at room temperature. The curve of one wafer-11 sensor is shown in blue. The curves of sensors from different positions on wafer-12 are shown in yellow, green, and red

3.1 Measurement setup

A laser beam was used as a signal source to explore the spatial resolution of the AC-LGAD sensor. The experimental setup is shown in the left plot of Fig. 7, and the plot on the right shows an image of the readout PCB board used in this study. In this setup, four contiguous strips on the sensor are tested using a transient current technique (TCT) platform, all of which are bonded to a specialized four-channel readout PCB board using aluminum wires. The wire-bonding locations are shown in Fig. 8. This particular four-channel readout PCB board was developed and manufactured at IHEP based on the design principles of a single-channel readout board originally crafted by the University of California Santa Cruz [43]. A high-speed SiGe transistor with a trans-impedance of approximately 470 Ω is used as the inverting amplifier on this board. This amplifier is followed by an external commercial amplifier with 10× voltage gain for each readout channel. As part of the experimental protocol, a bias voltage is applied through the back of the sensor, while the guard ring remains grounded. The operational voltage is set to −350 V (−150 V) for the wafer-11 (wafer-12) sensor, which is aligned with the specific characteristics observed in the *I*–*V* curve, as described in Sect. 2.1. Notably, this study confines its investigation to the 100 μm pitch design.

The laser is operated at a precise wavelength of 1064 nm, emitting pulses with a narrow width of 7.68 ps and frequency of 21.9 MHz. Its focused spot, which measures approximately 6 μm in diameter, can be dynamically maneuvered along both the *x*- and *y*-axes, facilitated by a sophisticated three-dimensional translation platform with an impressive positional accuracy of approximately 1 μm. To emulate the occurrence of single-photon events, an attenuator is positioned above the sensor, which reduced the energy of the laser beam to only 0.32% of its original intensity. The initiation of the signal transmission is synchronized with a pulse generated by the laser, subject to a potential trigger-time deviation of approximately 15 ps. Following amplification, the resultant signal pulses captured from the four wire-bonded strips are recorded using a state-of-the-art digital oscilloscope. This oscilloscope exhibits

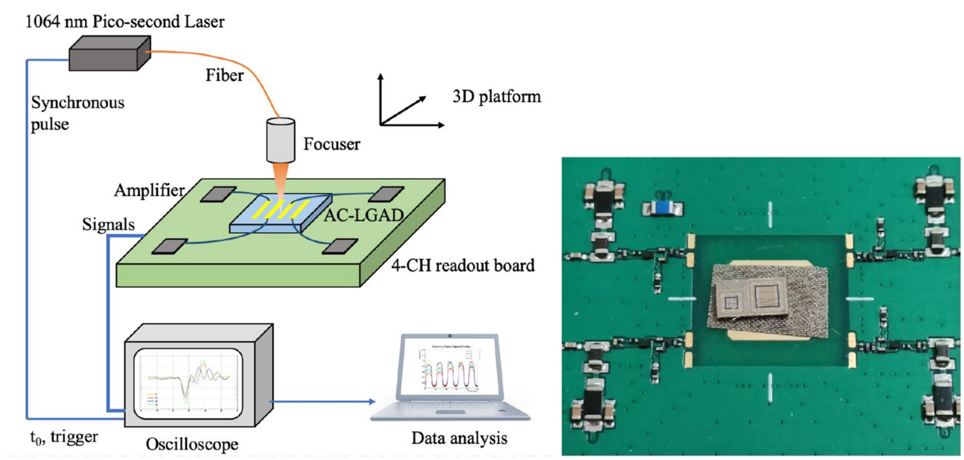

Fig. 7 (Color online) Equipment and wiring setup for the position test. Left: schematic diagram of the laser TCT platform. Right: picture of sensor bonded to a four-channel readout PCB board using aluminum wire

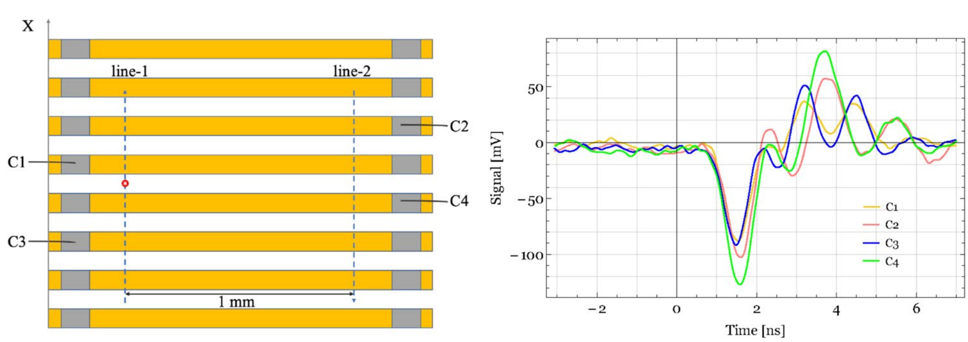

Fig. 8 (Color online) Left: Schematic of sensor strips. Two lines along the *x* coordinate indicate the paths along which the laser spot moves. C1–C4 represent the locations on the four strips wire bonded for the signal readout. Right: Waveforms of one trigger event. The yellow, red, blue, and green curves represent the four readout channels corresponding to C1, C2, C3, and C4, respectively

a remarkable sampling rate of 20 giga-samples per second (Gs/s) and bandwidth of 1 GHz.

The coordinate system of the measurements is established as follows: the x-axis is set perpendicular to the sensor strip, whereas $x = 0$ is set at the center of the gap between C1 and C4. The y-axis is set parallel to the sensor strips. The movement of the laser spot occurs with a precise step size of 2 μm, traversing along the x-axis in both the positive and negative directions relative to the strips, denoted as line-1 and line-2 in the left plot of Fig. 8, respectively. This adjustment facilitates the exploration of the variations in the signal waveform caused by the y position of the laser spot. To ensure a comprehensive analysis, a fixed separation of 1 mm is maintained between line-1 and line-2. This deliberate configuration enables scrutiny of the vertical impact of the laser spot on the signal waveform, with the y coordinate held constant throughout the measurement process. Each laser pulse triggers the oscilloscope approximately 1300 times during the data-acquisition phase. Within each triggered event, the oscilloscope captures four distinct signal pulses, each of which is represented by discernible peaks in the right plot of Fig. 8. Typically, these signal waveforms exhibit a narrow width of 1 ns. The amplitudes of these peaks vary depending on the spatial relationship between the readout strips and laser spot. Specifically, peaks of opposite polarity arise because of the migration of electrons within the n^+ layer toward the sensor periphery, as elaborated in prior research [40].

3.2 Position reconstruction and spatial resolution

The precise localization of the incoming signal, also known as the center of the laser spot, is regulated by a sophisticated three-dimensional translation platform with an impressive accuracy of up to 1 μm. The platform has a complex system of sensors and actuators that allow each movement to be performed with high precision. It tracks the charge depositions reconstructed from four distinct readout strips, with each deposition directly proportional to the spatial separation between the strips and the actual position of the signal. Consequently, the system capitalizes on any amplitude imbalance among the four adjacent readout strips to reconstruct the signal position with remarkable precision.

The plot on the left of Fig. 9 shows the average of the maximum amplitudes gathered by all the triggers at each step, providing insight into the signal strength across each channel corresponding to its position. This graphical representation serves as a window into the intricate dynamics within the system, offering a visual narrative of the journey of the signal from inception to detection. Additionally, the plot on the right of Fig. 8 shows a granular view of the signal collected by a single trigger at a specific location. The intricate movement of the photons and electrons is captured in detail, revealing the nuances that underpin the system operation. Notably, as the distance between the readout strip and laser spot increases, the signal amplitude decreases. This decline is further exacerbated when the laser spot encounters shading from the metal strips, causing the collected charge or signal amplitude to decrease to zero. Consequently, the rate of change in the signal amplitude reaches a turning point characterized by local maxima or minima at the periphery of the metal strips. The precise position of $x = 0$ is determined as the midpoint between the adjacent local maxima and minima, which is a feature of mathematical ingenuity that underscores the sophistication of the system. Leveraging this determined position as the central reference point, a range of

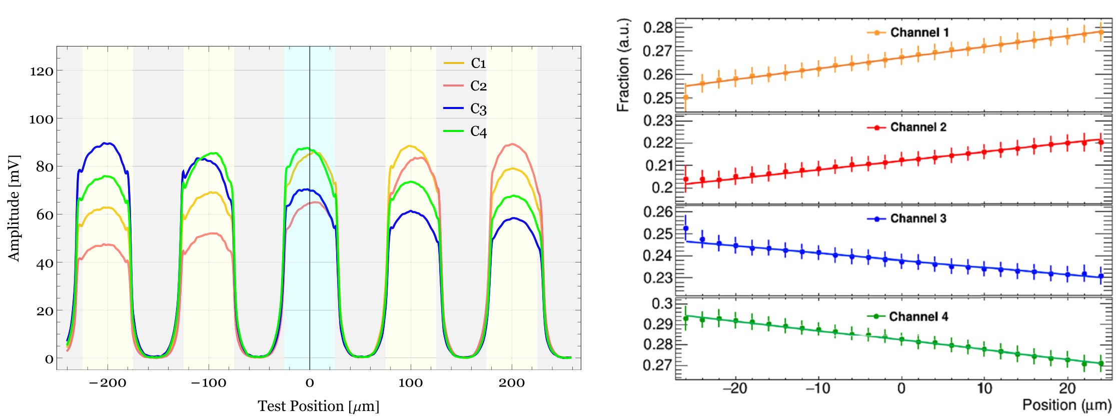

Fig. 9 (Color online) Left: Average maximum amplitudes with respect to the x coordinate, while $x = 0$ is set to be at the center of the gap where the laser hits. The absolute value of amplitudes after normalization are shown in the plot. Cyan-highlighted areas are selected for data analysis. Yellow-highlighted areas represent silicon gaps. All curves are measured with line-1 of the wafer-12 sensor. Right: Fraction of the maximum amplitude of each readout channel, averaged over all triggered events. Linear fits are applied to each fraction, as shown in the colored dashed lines. The yellow, red, blue, and green curves represent the four readout channels C1, C2, C3, and C4 of the oscilloscope, respectively

25 µm is meticulously selected both before and after $x = 0$ to compute the signal fraction with the highest accuracy and precision. This approach to data analysis ensures that every datapoint is scrutinized with care and attention to detail, befitting a scientific endeavor of this caliber.

A simplified linear model [44] that forms the basis for reconstructing the signal position assumes that the signal on each pad undergoes a linear decrease in intensity as the distance from the point of particle incidence increases. This linear model, while straightforward, offers a practical framework for understanding the signal behavior. In the context of strip sensors, where positional information is captured along a single dimension, typically recorded by four strip sensors, the complexity of signal analysis is simplified. As illustrated in the plot on the right of Fig. 8, the concept of signal fraction emerges, which is defined as the ratio of the maximum and minimum amplitudes detected on each channel to the minimum amplitude across all channels. By defining this fraction, the model further refines its predictive capacity, enabling the estimation of the positional variations within each strip. Therefore, we postulate that the signal fraction across each strip exhibits a linear relationship with the spatial distance from the impact point, which contributes to the effectiveness of the overarching linear model in reconstructing the signal position. The relationship between the impact position and signal fraction of each strip can be expressed as:

$$x = (f_i - \alpha_i)/\beta_i, i = 1, 2, 3, 4,$$

where x is the impact position, f_i is the signal fraction of each channel, α_i is the signal fraction of each channel at $x = 0$, and β_i is the rate of change in the signal fraction of each channel with respect to the impact position. We set $x = 0$ at the center of the gap between C1 and C4. This is achieved by determining the edges of the metal strip after deriving the signal distribution for each channel. The plot on the right of Fig. 9 shows the fraction of the maximum amplitude of each readout channel as a function of x, which is computed as follows:

$$f_i = \frac{A^i_{\max}}{A^1_{\max} + A^2_{\max} + A^3_{\max} + A^4_{\max}}, i = 1, 2, 3, 4,$$

where $A^i_{\max}$ is the maximum amplitude of each channel for a given x. A linear function is then used to fit the amplitude fraction of each channel. Therefore, four x values can be obtained from the fit function for any given event with the measured amplitude fraction (f_1, f_2, f_3, f_4), and the average of (x_1, x_2, x_3, x_4) is considered as the reconstructed laser-spot position.

At each specific position within the experimental setup, the measurement process is repeated a significant number of times, exceeding 1000 iterations. Subsequently, the statistical average of these measurements is computed, serving as the basis for determining the reconstructed positions. In the plots on the left of Fig. 10, a comprehensive distribution illustrating the reconstructed x coordinates is shown for a designated test position located at $x = 0$ µm. Notably, the distribution is characterized by two distinct curves, denoted by red and blue, which represent the positions derived from Gaussian fitting and reconstruction, respectively. Upon subjecting this distribution to a Gaussian-fit analysis, the mean value of -0.88ţm emerges as the determined reconstructed x, remarkably proximal to the actual $x = 0$ µm position. Moreover, the standard deviation computed at 9.63 µm via Gaussian fitting is indicative of the attained spatial resolution. The process of repeating measurements at various positions with the laser spot traversing the sensor surface yields a series of reconstructed positions, as shown in the plot on the right of Fig. 10. The reconstructed x-coordination positions are represented by blue and red dots, meticulously compared

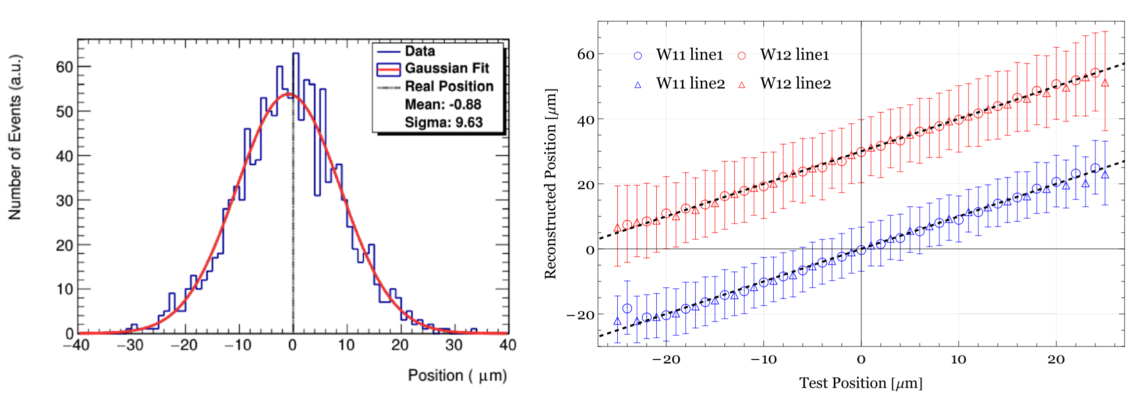

Fig. 10 (Color online) Left: Distribution of the reconstructed x coordinate for actual laser-spot position at $x = 0$ µm. The red curve shows a Gaussian fit to the distribution. Right: Reconstruction results of the two sensors from wafer-11 and wafer-12. The dashed line ($y = x$) represents the actual laser-spot position. The results of the wafer-12 sensor are shifted up by 30 µm for better demonstration

with the true laser-spot positions delineated by dashed lines corresponding to wafer-11 and wafer-12. Impressively, these reconstructed positions exhibit a high degree of conformity with the true positions, affirming the reliability and accuracy of the methodology employed.

A comprehensive and detailed analysis of the position-resolution measurement and its standard deviation is presented in Fig. 11, which provides valuable insights into the intricacies of this aspect. The left plot of Fig. 11 shows a nuanced depiction of the spatial resolution relative to x, exhibiting a significant range of variance spanning from 6.5 μm to 8.2 μm for wafer-11 and extending from 8.8 μm to 12.3 μm for wafer-12, respectively. This notable disparity in resolution underscores the superior performance of the wafer-11 sensor in comparison with wafer-12. This is largely attributable to the markedly lower n^+ dose (0.01 P) administered to wafer-11, as opposed to the 10 P dose allocated to wafer-12. Furthermore, the spatial resolution demonstrates a discernible decline toward the periphery of the gaps, as illustrated in the right plot of Fig. 11. This decrease in resolution can be ascribed to the inherent instability of the signal fraction as the laser spot approaches the metal strips, which introduces a variable that affects the precision of the measurements. Moreover, a subtle incongruity between the line-1 and line-2 measurements becomes apparent, primarily stemming from a similar phenomenon. The augmentation of readout channels is anticipated to ameliorate the reliance on spatial resolution and its standard deviation concerning the x-coordination, representing an avenue warranting thorough exploration in subsequent investigations and analyses.

4 Timing performance

The time performance of detectors based on the LGAD and AC-LGAD technologies is a critical aspect of their characterization, particularly in applications with high pile-up conditions. This was considered for the high-granularity timing detector of the ATLAS experiment and endcap timing layer of CMS experiment. Before and after hardness radiation, timing resolutions of 30 ps and 50 ps were achieved for the ATLAS high-granularity timing detector [32]. In the DarkSHINE experiment, the timing information was beneficial for the separation of multitrack and multi-interaction events. Thus, the timing resolution of the wafer-11 and wafer-12 sensors is studied and documented in this section.

The time performance of the AC-LGAD sensor is influenced by various factors, including the charge-collection time, transit-time spread, electronic noise, and intrinsic response of the sensor material. A systematic approach is employed to assess the time performance of the detector using pulsed-laser systems that emit photons with well-defined arrival times. The laser power is attenuated to mimic the charge deposition from a minimum-ionizing particle crossing the sensor under test, and the corresponding charge injection is considered uniform. In this case, The Landau fluctuation of the charge deposition along the path of the injected particle is assumed to be negligible. Therefore, the measured time resolution in the following text is dominated by the time-walk and jitter effects.

In accordance with the elucidation provided in Ref. [31], determination of the laser arrival time (herein referred to as t_{arrive} in the context of this study) entails a comprehensive expression derived from the averaging of the cross-threshold

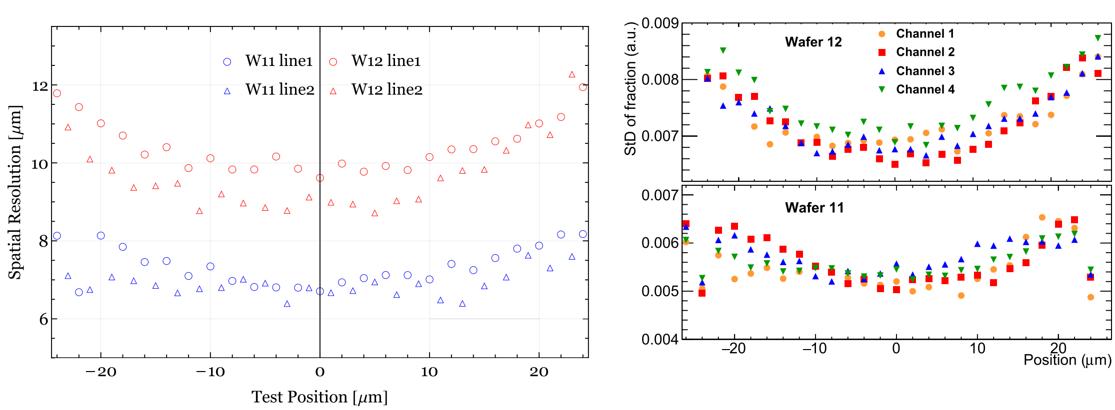

Fig. 11 (Color online) Left: Distribution of spatial resolution with respect to x coordinates. The blue and red marks represent the reconstructed position for the wafer-11 and wafer-12 sensor, respectively. The circle represents the measurement from line-1, and the triangle represents the measurement from line-2. Right: Distribution of the standard deviation of the signal fraction with respect to the x coordinate

time across four contiguous strips. This mathematical averaging is represented as

$$t_{\text{arrive}} = (t_1 + t_2 + t_3 + t_4)/4,$$

where each t_i term corresponds to the cross-threshold time of the Ci-th strip meticulously calibrated against a threshold level set at 30% of the rising edge, which is discerned from the waveform associated with the triggered event. Before the data analysis, the pedestal shapes are subtracted from the waveforms in each channel. Notably, the determination of the laser arrival time may undergo subtle shifts influenced by the inherent time performance of the strip sensors (designated as σ_{time}) and the intrinsic variability inherent in the trigger start time (referred to herein as σ_{t_0}). To mitigate these factors, the distribution of $(t_1 + t_2 - t_3 - t_4)/4$ is used to evaluate the time performance of the sensors instead of t_{arrive}. This judiciously chosen analytical approach thereby facilitates a comprehensive and nuanced evaluation of the time performance intricately associated with the strip sensors, particularly when the laser, in its trajectory, dynamically interfaces with the inter-strip gap region demarcated between C1 and C4, as visually depicted and elucidated in detail within the illustrative framework presented in Fig. 8 and meticulously appended to enhance clarity and visual comprehension. The standard deviation of this distribution is used to quantify the time performance:

$$\sigma_{\text{time}} = \sigma_{(t_1+t_2-t_3-t_4)/4}.$$

As an example, the plot on the left of Fig. 12 illustrates the distribution analysis of expression $(t_1 + t_2 - t_3 - t_4)/4$ for the wafer-11 sensor positioned at $x = 0$ μm in the line-1 measurement. An examination reveals the inherent variability in the performance characteristics of these sensors. Specifically, it provides insights into the temporal dynamics represented by the aforementioned expression, highlighting the subtle differences in their behavior at this particular spatial location. Notably, the measured time performance stands at 9.1 ps (11.3 ps) for the wafer-11 (wafer-12) sensor configuration at $x = 0$ μm. The plot on the right of Fig. 12 shows a more complete analysis considering all triggered events within both the line-1 and line-2 measurements. The average time performance is 8.3 ps (11.4 ps) for the wafer-11 (wafer-12) sensor combination. This assessment underscores the precision and reliability of the employed measurement techniques, offering a robust understanding of the temporal intricacies inherent in these sensor configurations. Moreover, these findings are consistent with those reported in Ref. [31], which reaffirms the validity and reproducibility of the experimental outcomes, thereby augmenting confidence in the observed results and their broader implications within the domain.

5 Conclusion

In summary, our investigation into the development and evaluation of the LGAD for the tracking system of the DarkSHINE experiment represents a significant leap forward in the field of particle-physics research. With the overarching goal of probing the mystery of dark matter by detecting dark photons and their invisible decay signatures, the DarkSHINE experiment requires cutting-edge technology capable of unprecedented precision and sensitivity. In this study, we detailed the design and performance evaluation of LGAD-based sensor modules to meet the stringent requirements of the DarkSHINE experiment. These modules were rigorously examined to assess their

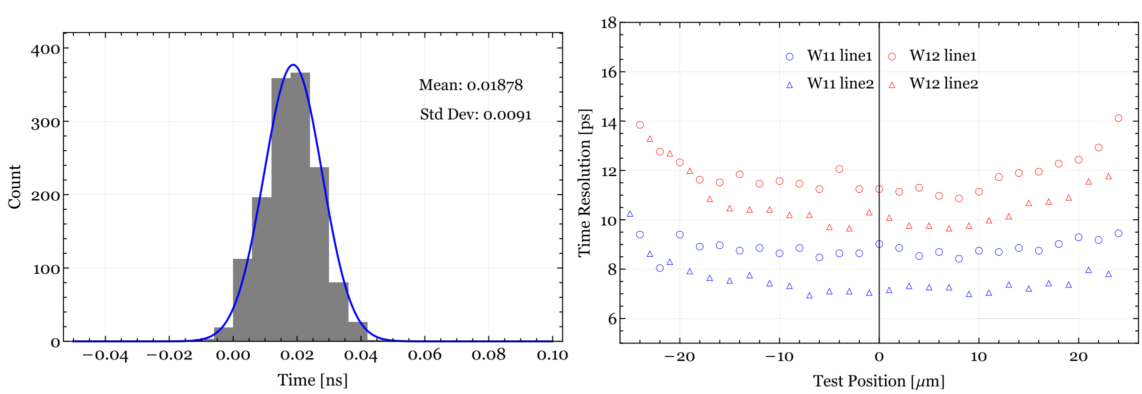

Fig. 12 (Color online) Left: Distribution of $(t_1 + t_2 - t_3 - t_4)/4$ concerning the wafer-11 sensor, line-1, positioned at $x = 0$ μm. Right: Distribution of time performance with respect to x coordinates. The blue and red marks represent the time performance of the wafer-11 and wafer-12 sensor, respectively. The circle represents the measurement from line-1, and the triangle represents the measurement from line-2

electrical characteristics and position-resolution and timing-measurement capabilities.

The successful fabrication of the two wafer-based sensor modules underscores the viability and scalability of AC-LGAD technology for high-precision tracking applications. Thorough testing of these modules revealed exceptional electrical performance, as evidenced by their stable *I*–*V* and *C*–*V* characteristics. Electrical reliability is crucial for ensuring the consistent and accurate operation of the tracking system under varying conditions. Furthermore, our experimental analyses demonstrate the outstanding position resolution achieved by the sensor modules. The range of spatial resolutions was 6.5 μm ~ 8.2 μm and 8.8 μm ~ 12.3 μm for the wafer-11 and wafer-12 sensors, respectively. The typical sensor-response time was approximately 1 ns. The wafer-11 sensor delivers better spatial resolution because of the smaller n^+ dose. Both the wafer-11 and wafer-12 sensors satisfied the requirements the DarkSHINE experiment. This level of precision enables the detection and localization of particle interactions with unprecedented accuracy, enhancing the ability of the experiment to discern subtle signals indicative of dark matter interactions. The timing-measurement resolutions of the sensors were 8.3 ps (11.4 ps) for the wafer-11 (wafer-12) sensor. The precise timing resolution achieved by the sensor modules facilitated the reconstruction of event sequences with high fidelity, further enhancing the sensitivity of the experiment to rare and elusive phenomena.

In conclusion, the findings presented in this study represent a significant step forward in the development of a tracking system for the DarkSHINE experiment. The use of AC-LGAD technology has achieved notable performance, enhancing the sensitivity and discovery potential of the experiment in the search for light dark matter candidates. Future research and continued refinement of the tracking system are important for advancing our understanding of the dark sector of the universe.

Author Contributions All authors contributed to the study conception and design. Material preparation, data collection and analysis were performed by Kang Liu, Meng-Zhao Li and Jun-Hua Zhang. The first draft of the manuscript was written by Yu-Feng Wang and Kun Liu, and all authors commented on previous versions of the manuscript. All authors read and approved the final manuscript.

Data availability The data that support the findings of this study are openly available in Science Data Bank at https://cstr.cn/31253.11.sciencedb.j00186.00292, and https://doi.org/10.57760/sciencedb.j00186.00292.

Declarations

Conflict of interest The authors declare that they have no competing interests.

References

1. X.Y. Ning, A. Abdukerim, Z.H. Bo et al., [PandaX], Limits on the luminance of dark matter from xenon recoil data. Nature **618**, 47–50 (2023). https://doi.org/10.1038/s41586-023-05982-0
2. Z.Y. Zhang, L.T. Yang, Q. Yue et al., [CDEX], Constraints on Sub-GeV dark matter-electron scattering from the CDEX-10 experiment. Phys. Rev. Lett. **129**, 221301 (2022). https://doi.org/10.1103/PhysRevLett.129.221301
3. E. Aprile, K. Abe, F. Agostini et al., [XENON], First dark matter search with nuclear recoils from the XENONnT experiment. Phys. Rev. Lett. **131**, 041003 (2023). https://doi.org/10.1103/PhysRevLett.131.041003
4. The ATLAS collaboration, Dark matter summary plots for s-channel, 2HDM+a, Higgs portal and Dark Higgs models. ATL-PHYS-PUB-2023-018
5. A. Hayrapetyan, A. Tumasyan, W. Adam et al., [CMS], Search for inelastic dark matter in events with two displaced muons and missing transverse momentum in proton-proton collisions at $\sqrt{s}$ =13 TeV. Phys. Rev. Lett. **132**, 041802 (2024). https://doi.org/10.1103/PhysRevLett.132.041802
6. DAMPE Collaboration, Detection of spectral hardenings in cosmic-ray boron-to-carbon and boron-to-oxygen flux ratios with DAMPE. Sci. Bull. **67**, 2162–2166 (2022). https://doi.org/10.1016/j.scib.2022.10.002
7. M. Aguilar, G. Ambrosi, H. Anderson et al., [AMS], Temporal structures in positron spectra and charge-sign effects in galactic cosmic rays. Phys. Rev. Lett. **131**, 151002 (2023). https://doi.org/10.1103/PhysRevLett.131.151002
8. European Strategy Group, 2020 Update of the European strategy for particle physics. CERN-ESU-013, CERN-ESU-015 (2020). https://doi.org/10.17181/ESU2020
9. J.N. Butler, R.S. Chivukula, A. de Gouvêa et al., Report of the 2021 U.S. community study on the future of particle physics (Snowmass 2021). https://doi.org/10.2172/1922503
10. B. Holdom, Two U(1)'s and epsilon charge shifts. Phys. Lett. B **166**, 196–198 (1986). https://doi.org/10.1016/0370-2693(86)91377-8
11. R. Foot, X.G. He, Comment on Z Z' mixing in extended gauge theories. Phys. Lett. B **267**, 509–512 (1991). https://doi.org/10.1016/0370-2693(91)90901-2
12. K. Fuyuto, X.G. He, G. Li et al., CP-violating dark photon interaction. Phys. Rev. D **101**, 075016 (2020). https://doi.org/10.1103/PhysRevD.101.075016
13. G. Choi, T.T. Yanagida, N. Yokozaki, Dark photon dark matter in the minimal B-L model. JHEP **01**, 057 (2021). https://doi.org/10.1007/JHEP01(2021)057
14. Y. Cheng, X.G. He, M.J. Ramsey-Musolf et al., CP-violating dark photon kinetic mixing and type-III seesaw model. Phys. Rev. D **105**, 095010 (2022). https://doi.org/10.1103/PhysRevD.105.095010. [arXiv:2104.11563 [hep-ph]]
15. S.F. Ge, X.D. Ma, P. Pasquini, Probing the dark axion portal with muon anomalous magnetic moment. Eur. Phys. J. C **81**, 787 (2021). https://doi.org/10.1140/epjc/s10052-021-09571-1
16. B. Yan, Probing the dark photon via polarized DIS scattering at the HERA and EIC. Phys. Lett. B **833**, 137384 (2022). https://doi.org/10.1016/j.physletb.2022.137384
17. M. Ablikim et al., [BESIII], Search for invisible decays of a dark photon using e^+e^- annihilation data at BESIII. Phys. Lett. B **839**, 137785 (2023). https://doi.org/10.1016/j.physletb.2023.137785
18. C. Ahdida et al., [SHiP], Sensitivity of the SHiP experiment to dark photons decaying to a pair of charged particles. Eur. Phys. J. C **81**, 451 (2021). https://doi.org/10.1140/epjc/s10052-021-09224-3

19. X.G. Wang, A.W. Thomas, Dark photon effect on the rare kaon decay. J. Phys. G **50**, 085001 (2023). https://doi.org/10.1088/1361-6471/acdfed
20. C.W. Chiang, P.Y. Tseng, Probing a dark photon using rare leptonic kaon and pion decays. Phys. Lett. B **767**, 289–294 (2017). https://doi.org/10.1016/j.physletb.2017.02.022
21. H. An, M. Pospelov, J. Pradler et al., Direct detection constraints on dark photon dark matter. Phys. Lett. B **747**, 331–338 (2015). https://doi.org/10.1016/j.physletb.2015.06.018
22. M. Fabbrichesi, E. Gabrielli, G. Lanfranchi, The physics of dark photon.(Springer, Switzerland AG, 2021) https://doi.org/10.1007/978-3-030-62519-1
23. F. Zhou, C. Adolphsen, A. Benwell et al., Commissioning of the SLAC Linac Coherent Light Source II electron source. Phys. Rev. Accel. Beams **24**, 073401 (2021). https://doi.org/10.1103/PhysRevAccelBeams.24.073401
24. R. England, K. Bane, M. Borland et al., Multibunch studies for LCLS-II high energy upgrade. https://doi.org/10.18429/JACoW-IPAC2021-THPAB220
25. M. Santana Leitner, J.C. Liu, S.X. Mao et al., Radiation protection aspects in the design of the Linac Coherent Light Source II. Prog. Nucl. Sci. Tech. **4**, 169–172 (2014). https://doi.org/10.15669/pnst.4.169
26. J. Wan, Y. Leng, B. Gao et al., Simulation of wire scanner for high repetition free electron laser facilities. Nucl. Instrum. Meth. A **1026**, 166200 (2022). https://doi.org/10.1016/j.nima.2021.166200
27. Z.T. Zhao, C. Feng, K.Q. Zhang, Two-stage EEHG for coherent hard X-ray generation based on a superconducting linac. Nucl. Sci. Tech. **28**, 117 (2017). https://doi.org/10.1007/s41365-017-0258-z
28. Z.T. Zhao, C. Feng, J.H. Chen et al., Two-beam based two-stage EEHG-FEL for coherent hard X-ray generation. Science Bulletin **61**(117), 720–727 (2016). https://doi.org/10.1007/s11434-016-1060-8
29. Z. Zhao, D. Wang, Z.H. Yang et al., SCLF: An 8-GeV CW scfr linac-based X-Ray FEL facility in Shanghai. https://doi.org/10.18429/JACoW-FEL2017-MOP055
30. J. Chen, Y.F. Wang, Y.L. Zhang et al., Prospective study of light dark matter search with a newly proposed DarkSHINE experiment. Sci. China Phys. Mech. Astron. **66**, 211062 (2023)
31. M. Li, W. Sun, Z. Liang et al., The performance of large-pitch AC-LGAD with different N+ dose. IEEE Trans. Nucl. Sci. **70**, 2134–2138 (2023). https://doi.org/10.1109/TNS.2023.3289032
32. X. Shi, M.K. Ayoub, J. Barreiro Guimarães da Costa et al., Radiation campaign of HPK prototype LGAD sensors for the High-Granularity Timing Detector (HGTD). Nucl. Instrum. Meth. A **979**, 164382 (2020). https://doi.org/10.1016/j.nima.2020.164382
33. X. Zhang, Y. Liu, Y. Shao et al., One-dimensional position-sensitive LGAD with a DC coupled and resistive charge division mechanism. IEEE Trans. Nucl. Sci. **70**, 853–858 (2023). https://doi.org/10.1109/TNS.2023.3264661
34. S. Kita, K. Nakamura, T. Ueda et al., Optimization of capacitively coupled Low Gain Avalanche Diode (AC-LGAD) sensors for precise time and spatial resolution. Nucl. Instrum. Meth. A **1048**, 168009 (2023). https://doi.org/10.1016/j.nima.2022.168009
35. J. Ott, S. Letts, A. Molnar et al., Investigation of signal characteristics and charge sharing in AC-LGADs with laser and test beam measurements. Nucl. Instrum. Meth. A **1045**, 167541 (2023). https://doi.org/10.1016/j.nima.2022.167541
36. M. Li, H. Cui, Y. Fan et al., The timing resolution of IHEP-NDL LGAD sensors with different active layer thicknesses. IEEE Trans. Nucl. Sci. **68**, 2309–2314 (2021). https://doi.org/10.1109/TNS.2021.3097746
37. H.F.W. Sadrozinski, S. Ely, V. Fadeyev et al., Ultra-fast silicon detectors. Nucl. Instrum. Meth. A **730**, 226 (2013). https://doi.org/10.1016/j.nima.2013.06.033
38. ATLAS collaboration, Technical proposal: a high-granularity timing detector for the ATLAS phase-II upgrade. CERN-LHCC-2018-023
39. CMS collaboration, Technical proposal for a MIP timing detector in the CMS experiment phase 2 upgrade, CERN-LHCC-2017-027
40. G. Giacomini, W. Chen, G. D'Amen et al., Fabrication and performance of AC-coupled LGADs. JINST **14**, P09004 (2019). https://doi.org/10.1088/1748-0221/14/09/P09004
41. X. Yang, S. Alderweireldt, N. Atanov et al., Layout and performance of HPK prototype LGAD sensors for the high-granularity timing detector. Nucl. Instrum. Meth. A **980**, 164379 (2020). https://doi.org/10.1016/j.nima.2020.164379
42. Alexander Chilingarov, Lancaster University, RD50-Recommendations for performing measurements(Part I: IV and CV measurements in Si diodes), RD50 Technical Note RD50-2003-03
43. N. Cartiglia, A. Staiano, V. Sola et al., Beam test results of a 16 ps timing system based on ultra-fast silicon detectors. Nucl. Instrum. Methods A **850**, 83–88 (2017). https://doi.org/10.1016/j.nima.2017.01.021
44. M. Tornago, R. Arcidiacono, N. Cartiglia et al., Resistive AC-coupled silicon detectors: principles of operation and first results from a combined analysis of beam test and laser data. Nucl. Instrum. Methods A **1003**, 165319 (2021). https://doi.org/10.1016/j.nima.2021.165319